International Journal of Heat and Mass Transfer 52 (2009) 3205–3216

Contents lists available at ScienceDirect

International Journal of Heat and Mass Transfer

journal homepage: www.elsevier.com/locate/ijhmt

Numerical investigation of heat and fluid flow across a rotating circular cylinder maintained at constant temperature in 2-D laminar flow regime

Sachin B. Paramane, Atul Sharma *

Department of Mechanical Engineering, Indian Institute of Technology Bombay, Mumbai 400076, India

ARTICLE INFO

Article history:
Received 18 February 2008
Received in revised form 9 September 2008
Accepted 24 December 2008
Available online 30 March 2009

Keywords:
Rotation rate
Heatline
Flow transitions
Drag reduction
Heat transfer suppression

ABSTRACT

Forced convection heat transfer across a circular cylinder rotating with a constant non-dimensional rotation rate (α) varying from 0 to 6 are investigated for Reynolds numbers of 20–160 and a Prandtl number of 0.7. Flow transitions is reported here for a wider range of Reynolds number and rotation rates. Heat transfer visualization technique using heatlines is implemented here, probably for the first time, in finite volume framework for the unsteady heat transfer problem in complex domain and used for heat flow analysis. Rotation can be used as a drag reduction and heat transfer suppression technique.

1. Introduction

Classical problem of flow and heat transfer past a stationary circular cylinder has been subject of numerous investigations [1]. In contrast, such studies on the cylinder subjected to rotation are scarce although this particular technique is used for flow control, lift enhancement, boundary layer control etc. In these flows, the results depend not only on the Reynolds number (Re) but also on rotation rate (α) defined as the ratio of rotational velocity of the cylinder wall to the incoming free stream flow velocity, expressed as

$$\mathrm{Re} = \frac{u_\infty D}{\nu} \text{ and } \alpha = \frac{D\omega}{2u_\infty} \tag{1}$$

The flow across a stationary cylinder undergoes various transition with increasing Re such as steady to periodic flow at Re = 47 and 2-D periodic to 3-D periodic flow at Re = 188.5 reported by Barkley and Henderson [2] and at Re = 194 by Williamson [3]. Baranyi [4] predicted the 3-D transition at Re = 160 for the cylinder. Thus, the present study is limited to $\mathrm{Re} \leqslant 160$ in the 2-D laminar flow regime for the cylinder subjected to various rotation rates. Table 1 gives a brief overview of published studies on flow and heat transfer including the range of Re and α values, grid sizes and domain height. An excellent review for this problem is given in Stojkovic et al. [10] and Mittal and Kumar [12]. Suppression of vortex shedding at a critical rotation rate $\alpha > \alpha_l$ for a $\mathrm{Re} > 47$ was first predicted by Hu et al. [14]. Thereafter, around same time, Stojkovic et al. [10,11] at Re = 60, 100 and 200 and Mittal and Kumar [12] at Re = 200 found two more flow transitions. Second transition from steady to unsteady flow at α_{II} and third transition at $\alpha > \alpha_{III}$ where unsteady flow is again suppressed to steady flow. They found the second unsteady flow mode in a very narrow range of $\alpha(\alpha_{II} \leqslant \alpha \leqslant \alpha_{III})$. Kang et al. [9] found drag and lift coefficient decreases with increase in rotation rates.

Badr and Dennis [13] found a decrease in laminar forced convection heat transfer with increasing rotation rate from an isothermal cylinder for Re = 5, 10, 20, 40 and 100 at $\alpha \leqslant 4$. An approximate analytical derivation for average Nusselt number was obtained by Kendoush [15] using the appropriate velocity components in the energy equation. Table 1 shows that all work on rotating circular cylinder was done for isothermal flow except that of Badr and Dennis [13] for heat transfer. The objective of present study is to develop an in-house multi-block finite volume code for complex domains on a collocated grid and a detailed investigation of flow and heat transfer characteristics of rotating circular cylinder for wide range of Reynolds number ($20 \leqslant \mathrm{Re} \leqslant 160$) and rotation parameters ($0 \leqslant \alpha \leqslant 6$) in the two-dimensional laminar flow regime. Furthermore, the objective is to analyse the heat flow using heatline visualization technique (proposed by Kimura and Bejan [16]) implemented in finite volume framework for both steady and unsteady periodic flows.

2. Physical description of the problem

The flow configuration is shown in Fig. 1(a). A two-dimensional circular cylinder with diameter D exposed to a constant

* Corresponding author. Tel.: +91 22 2576 7505; fax: +91 22 25726875.
E-mail address: atuls@me.iitb.ac.in (A. Sharma).

0017-9310/$ - see front matter © 2009 Elsevier Ltd. All rights reserved.
doi:10.1016/j.ijheatmasstransfer.2008.12.031

Nomenclature

C_D	total drag coefficient ($= C_{Dp} + C_{Dv}$)
C_{Dp}	pressure drag coefficient ($= F_{Dp}/\frac{1}{2}\rho u_\infty^2 D$)
C_{Dv}	viscous drag coefficient ($= F_{Dv}/\frac{1}{2}\rho u_\infty^2 D$)
C_L	total Lift coefficient ($= C_{Lp} + C_{Lv}$)
C_{Lp}	pressure lift coefficient ($= F_{Lp}/\frac{1}{2}\rho u_\infty^2 D$)
C_{Lv}	viscous lift coefficient ($= F_{Lv}/\frac{1}{2}\rho u_\infty^2 D$)
f	frequency of vortex shedding, s^{-1}
F_{Dp}	pressure drag force on the cylinder
F_{Dv}	viscous drag force on the cylinder
F_{Lp}	pressure lift force on the cylinder
F_{Lv}	viscous lift force on the cylinder
H	heat function
M	number of grid points in radial direction
N	number of grid points in angular direction
n	cylinder surface normal direction
Nu	average Nusselt number
Nu_0	average Nusselt number for stationary cylinder
Nu_L	local Nusselt number ($= -\frac{\partial\theta}{\partial n}$)
St	non-dimensional vortex-shedding frequency ($= fD/u_\infty$)
T_∞	free-surface temperature, K
u	streamwise velocity, $m\,s^{-1}$
u_∞	free-stream velocity, $m\,s^{-1}$
U	non-dimensional streamwise velocity ($= u/u_\infty$)
v	cross-stream velocity, $m\,s^{-1}$
V	non-dimensional cross-stream velocity ($= v/u_\infty$)
x	streamwise dimension of coordinates, m
X	non-dimensional streamwise dimension of coordinates ($= x/D$)
y	cross-stream dimension of coordinates, m
Y	non-dimensional cross-stream dimension of coordinates ($= y/D$)

Greek symbols

α	non-dimensional rotation rate ($= D\omega/2u_\infty$)
ϕ	angular displacement from the front stagnation point, °
ψ	stream function
τ	non-dimensional time
θ	non-dimensional temperature
ω	constant angular velocity of the cylinder rotation, $rad\,s^{-1}$

Subscripts

W	surface of the cylinder
rms	root mean square

free-stream velocity and temperature represented by u_∞ and T_∞, respectively. Cylinder is rotating in a counterclockwise direction with constant angular velocity ω and maintained at a constant temperature $T_W > T_\infty$. Kang et al. [9] and Stojkovic et al. [10] carried out the numerical investigation for rotating cylinder placed at the center of a square domain of size 100D which was found sufficient enough in the present study for domain independent results and is used here.

3. Governing equations and boundary conditions

The unsteady, conservative and dimensionless form of the Navier–Stokes equations in two dimensions for the incompressible flow (with constant thermo-physical property) are the governing equations:

Continuity:

$$\frac{\partial U}{\partial X} + \frac{\partial V}{\partial Y} = 0 \tag{2}$$

X-momentum:

$$\frac{\partial U}{\partial \tau} + \frac{\partial (UU)}{\partial X} + \frac{\partial (VU)}{\partial Y} = -\frac{\partial P}{\partial X} + \frac{1}{\mathrm{Re}}\left(\frac{\partial^2 U}{\partial X^2} + \frac{\partial^2 U}{\partial Y^2}\right) \tag{3}$$

Y-momentum:

$$\frac{\partial V}{\partial \tau} + \frac{\partial (UV)}{\partial X} + \frac{\partial (VV)}{\partial Y} = -\frac{\partial P}{\partial Y} + \frac{1}{\mathrm{Re}}\left(\frac{\partial^2 V}{\partial X^2} + \frac{\partial^2 V}{\partial Y^2}\right) \tag{4}$$

Thermal-energy equation:

$$\frac{\partial \theta}{\partial \tau} + \frac{\partial (U\theta)}{\partial X} + \frac{\partial (V\theta)}{\partial Y} = \frac{1}{\mathrm{RePr}}\left(\frac{\partial^2 \theta}{\partial X^2} + \frac{\partial^2 \theta}{\partial Y^2}\right) \tag{5}$$

with

$$U = \frac{u}{u_\infty}, \quad V = \frac{v}{u_\infty}, \quad \tau = \frac{t u_\infty}{D}, \quad X = \frac{x}{D}, \quad Y = \frac{y}{D},$$
$$P = \frac{p}{\rho u_\infty^2}, \quad \theta = \frac{T - T_\infty}{T_W - T_\infty}$$

Here u_∞ and T_∞ is the uniform velocity and temperature of the fluid far away from the cylinder. The Reynolds number and Prandtl number are the governing parameters for this problem and is defined as $\mathrm{Re} = \rho u_\infty D/\mu$ and $\mathrm{Pr} = \mu c_p/k$.

Boundary conditions for the flow and temperature field are as follows:

Left boundary (inlet): uniform flow condition

$$U = 1, \quad V = 0, \quad \frac{\partial P}{\partial X} = 0 \quad \text{and} \quad \theta = 0 \tag{6}$$

Table 1
Summary of literature survey for flow and heat transfer across a rotating circular cylinder. Note that except the last one, all the other work are for isothermal flow.

Author	Reynolds number	Rotation rate	Grid size	Domain height
Townsend [5]	10, 40, 60	$0 \leqslant \alpha \leqslant 5$	$M = 20, N = 40$	$H/D = 20.1$
Badr et al. [6]	5, 20, 60, 100, 200	$0 \leqslant \alpha \leqslant 1$	$M \leqslant 41, N \leqslant 162$	$H/D = 400$
Ingham and Tang [7]	5, 20	$0 \leqslant \alpha \leqslant 3$	$42 \leqslant N \leqslant 162, 11 \leqslant M \leqslant 41$	$H/D \to \infty$
Tang and Ingham [8]	60, 100	$0 \leqslant \alpha \leqslant 1$	$M \leqslant 60, N \leqslant 30$	$H/D \to \infty$
Kang et al. [9]	40, 60, 100, 160	$0 \leqslant \alpha \leqslant 2.5$	$M = 241, N = 241$	$H/D = 100$
Stojkovic et al. [10]	$0.01 \leqslant Re \leqslant 45, 100$	$0 \leqslant \alpha \leqslant 6, \leqslant 12$	$8.10^5, M = 241, N = 241$	$H/D = 10^3, H/D = 100$
Stojkovic et al. [11]	60, 160, 200	$0 \leqslant \alpha \leqslant 6$	$M = 241, N = 241$	$H/D = 100$
Mittal and Kumar [12]	200	$0 \leqslant \alpha \leqslant 5$	32,190 nodes	$H/D = 200$
Badr and Dennis [13]	$5 \leqslant Re \leqslant 100$	$0.1 \leqslant \alpha \leqslant 4$	$M \leqslant 41, N \leqslant 162$	$H/D = 400$

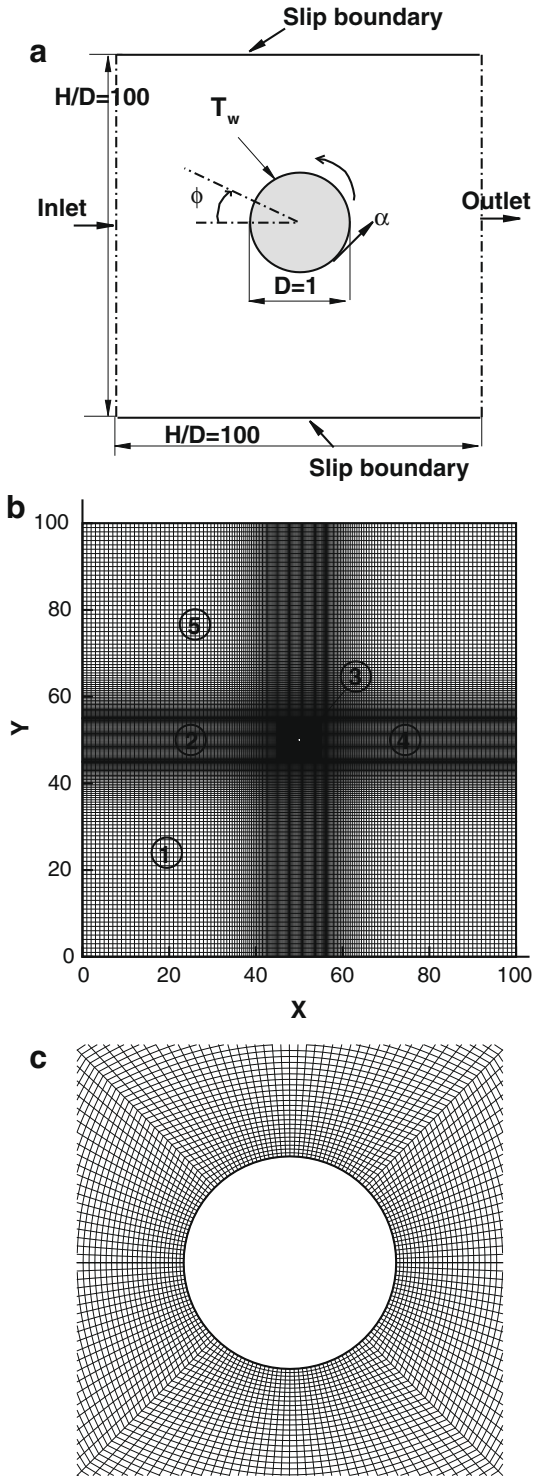

Fig. 1. (a) Schematic of the unconfined flow and heat transfer around rotating circular cylinder. (b) Grid structure. (c) Close up view in the vicinity of cylinder.

Top and bottom boundary: free slip flow condition

$$\frac{\partial U}{\partial Y}=0, V=0, \frac{\partial P}{\partial Y}=0, \text{and } \frac{\partial \theta}{\partial Y}=0 \tag{7}$$

Right boundary (outlet): convective boundary condition

$$\frac{\partial \chi}{\partial \tau}+U_c\frac{\partial \chi}{\partial n}=0, P=0 \tag{8}$$

where, $U_c=1, \chi=U, V$ and θ

Solid surface of the cylinder: Dirichlet boundary condition

$$U=-\alpha sin(\phi), V=-\alpha cos(\phi), \frac{\partial P}{\partial n}=0, \theta=1 \tag{9}$$

4. Numerical method

In the present study multi-block structured grid is developed by dividing the domain into five blocks as shown in Fig. 1(b). A preliminary investigation is conducted using various types of stretching functions, to determine the grid that best captured the unsteady flow features present in the flow calculations. The grid structure with total number of control volumes 43076 which gave the best results after a grid independent study is finally used. The grid is divided into four zones in both directions and uniform as well as non-uniform grid distributions are employed. The elliptic grid generation technique is used for generation of grid for third block in which cylinder is placed with a very fine grid of 0.02 in the radial direction clustered around the cylinder over a distance of 0.5 units to adequately capture wake-wall interactions. On the surface of the cylinder a uniform cell size of 0.02 is used in the angular direction. Close up view in the vicinity of cylinder is shown in Fig. 1(c). A time-step of 10^{-4}, is found sufficient to obtain time-step independent unsteady results.

A Semi-explicit finite-volume method by Sharma and Eswaran [17] for complex 2-D geometries on a non-staggered grid is used. For complex geometry, the normal gradient of a variable at a face center of a CV is computed in terms of two components: First, gradient along the line joining cell centers (on either side of the face) and second, gradient tangential to the face. The first component uses the cell center values and the second one uses the cell vertex values (obtained by volume weighted linear interpolation of the adjoining four cell center values). Quadratic Upwind Interpolation for Convective Kinematics (QUICK) convection scheme is consistently implemented in the code while ensuring the conservative property of the finite volume method. In the previous work by present authors (Paramane and Sharma [18]), implementation issues for higher order convection scheme on non-staggered grid is discussed and QUICK convection scheme is shown better than first/second order and central difference scheme.

Barnes [19] reported experimental results at Re = 60 for $0 \leqslant \alpha \leqslant 1.2$ in excellent agreement with the numerical results of Kang et al. [9] and strong disagreement with the results of Hu et al. [14]. Strouhal number, $St = 0.1359$ is found in the present work at Re = 60 and $\alpha = 1$ which matches very well with the experimental value of 0.1372, obtained by Barnes [19]. The present numerical method is also validated against the results of Kang et al. [9] and Stojkovic et al. [10] and an excellent agreement is shown in Table 2.

5. Heat-function and heatlines

Traditionally, temperature-contours/isotherms are used to describe heat transfer characteristics whereas for fluid flow, velocity contours are not usually used but streamlines are more common. Isotherms and streamlines together do not visually describe

Table 2
Comparison of present results with the published results for Re = 100 at $\alpha = 1$ and 2.

Source	Kang et al. [9]		Stojkovic et al. [10]		Present	
Parameter	$\alpha=1$	$\alpha=2$	$\alpha=1$	$\alpha=2$	$\alpha=1$	$\alpha=2$
St	0.1655	–	0.1658	–	0.1645	–
C_L	−2.4881	−5.4931	−2.504	−5.48	−2.49	−5.4757
C_D	1.1040	0.4682	1.1080	0.46	1.0951	0.4683
C'_L	0.3631	–	0.3616	–	0.3461	–
C'_D	0.099	–	0.0986	–	0.0981	–

relationship between heat and fluid flow mechanisms. Kimura and Bejan [16] in 1983, first proposed heatlines as an adequate tool for analysis of 2D convective heat transfer. Thereafter, most of the researchers [20–23] have used the technique for steady flows and natural convection problem but not for the unsteady forced convection flows considered here.

The dimensionless form of heat function H is defined as:

$$\frac{\partial H}{\partial Y} = \mathrm{Pe}U\theta - \frac{\partial \theta}{\partial X} \tag{10}$$

$$-\frac{\partial H}{\partial X} = \mathrm{Pe}V\theta - \frac{\partial \theta}{\partial Y} \tag{11}$$

where $\mathrm{Pe} = u_\infty D/\alpha = \mathrm{RePr}$ and the heat function is non-dimensionalised by $\rho c_p (T_W - T_\infty) u_\infty D/\mathrm{Pe}$. Heatline represents a combination of *thermal-diffusion/conduction* and *enthalpy/advection* flow referred here as "heat/thermal-energy flow". According to *caloric theory* of the famous French scientist Antonie Lavoisier, heat is considered as an inviscible, tasteless, odourless, weightless fluid, which he called *caloric fluid*. Although, the modern interpretation of heat is somewhat different, nevertheless, there are certain problems involving heat flow such as discussion on heatlines here for which Lavoisier's approach is rather useful. The role of heatlines for heat flow is analogous to that of streamlines for fluid flow: difference of stream/heat function values represents fluid/heat flow rate i.e. the function remains constant on a solid/adiabatic wall, tangent to stream/heat line represents the direction of fluid/heat flow with no flow in the normal direction and the stream/heat line originate or emerge at the mass/heat source. For the cylinder surface maintained at CWT smaller than the inlet fluid temperature, then heat source is also at inlet and heat sink is at the surface otherwise heat source is at the cylinder surface, the case considered here. The use of heatline for unsteady incompressible flow is analogous to the use of streamline for unsteady compressible flow. This is because the energy equation for incompressible and continuity equation for the compressible flow are not divergence free as the unsteady terms acts like a volumetric source term.

All the researchers mentioned above solved the Poisson type of heat function equation (obtained by eliminating the temperature gradient in Eqs. (10) and (11) by cross-differentiation) for simple geometry/domain problems using boundary conditions for heat functions to get the value of heat function variation in the computational domain. In the present study, probably for the first time, the heat function equation is computed at each time step in the *finite-volume method framework* as well as that for the *complex geometry/domain* (except that of Dalal and Das [23]) where Eqs. (10) and (11) are integrated to calculate the heat function at the cell vertex from the already computed convection and diffusion fluxes on the faces of the cells. This method reduces the complexity and effort for the formulation of boundary conditions and solving the heat function Poisson equation. The heat function formulation is validated and an excellent agreement with the results of Deng and Tang [21] is found.

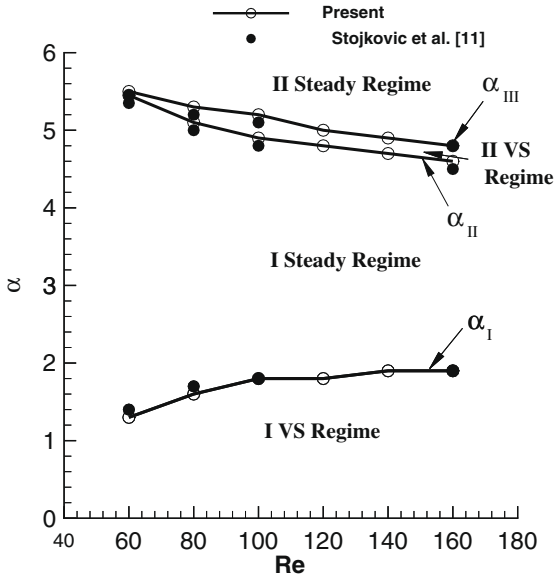

Fig. 2. Stability map for various Re and rotation rates α, demarcating the steady and unsteady periodic flow regimes.

6. Results and discussion

In the present study, the governing parameters considered are as follows:
Re = 20–160 in the steps of 20.
Rotation rate (α): 0–6.
Prandtl number has been fixed at 0.7 (as for air).

6.1. Flow transitions

For $\mathrm{Re} > 60$ Fig. 2 shows a stability map with the three curves representing the rotation rates (α_I, α_{II} and α_{III}) at which three transitions between steady and unsteady flows with the four flow regimes are found: I VS (vortex shedding) regime for $\alpha \leqslant \alpha_I$, I Steady regime at $\alpha_I < \alpha < \alpha_{II}$, II VS (vortex shedding) regime at $\alpha_{II} \leqslant \alpha \leqslant \alpha_{III}$ and II Steady regime for $\alpha > \alpha_{III}$. Thus for a Re in the vortex shedding regime of the stationary cylinder, the suppression of vortex shedding occurs at certain rotation rate for a rotating cylinder and flow remains steady at higher rotation rates except for a narrow range of α at which vortex shedding reappears. No such transitions with increasing rotation rate is found and flow remains steady for Re = 20 and 40. Furthermore, with increasing Re, it can be seen that α_I increases monotonically but α_{II} and α_{III} decreases. The difference between α_{II} and α_{III} decreases monotonically with Re decreasing from 100 to 60 with $\alpha_{II} = 5.45$ and $\alpha_{III} = 5.5$ at $\mathrm{Re} = 60$. This may be the reason that incipience of vortex shedding is not found at $\mathrm{Re} = 40$ for α as high as 20 in the present work. The figure also shows a good agreement between the present results and that of Stojkovic et al. [11].

6.2. Heat and fluid flow model

To make the discussion in the following subsections more clear, steady heat/fluid flow patterns represented by heat/stream lines for the stationary and rotating cylinder are compared in this subsection at Re = 40. The comparison for fluid flow is done with the help of points such as center and saddles proposed by Perry et al. [24] and Eaton [25]. Saddle point are critical points where streamline crosses itself and are called viscous or inviscid depending on whether they are on solid-surface or in the flow-field, respectively. Fig. 3(a) shows "k" and "l" as the two viscous saddle points for the stationary and two inviscid ones for the rotating cylinder at $\alpha = 1$, shown in Fig. 3(b). Fig. 3(c) shows only one inviscid saddle point "k" at the highest rotation rate. A streamline that contains an inviscid saddle point referred as a "separatrix" is also shown in the figure by thick line.

Fig. 3(a) shows twin vortex, upper and lower represented by "A" and "B", attached to the rear end of the cylinder surface whereas Fig. 3(b) shows the merging of lower counter-clockwise vortex with the cylinder counter-clockwise rotation to form a vortex around the cylinder called here as *"enveloping vortex"* while upper clockwise vortex called here as *"detached vortex"* is seen detached

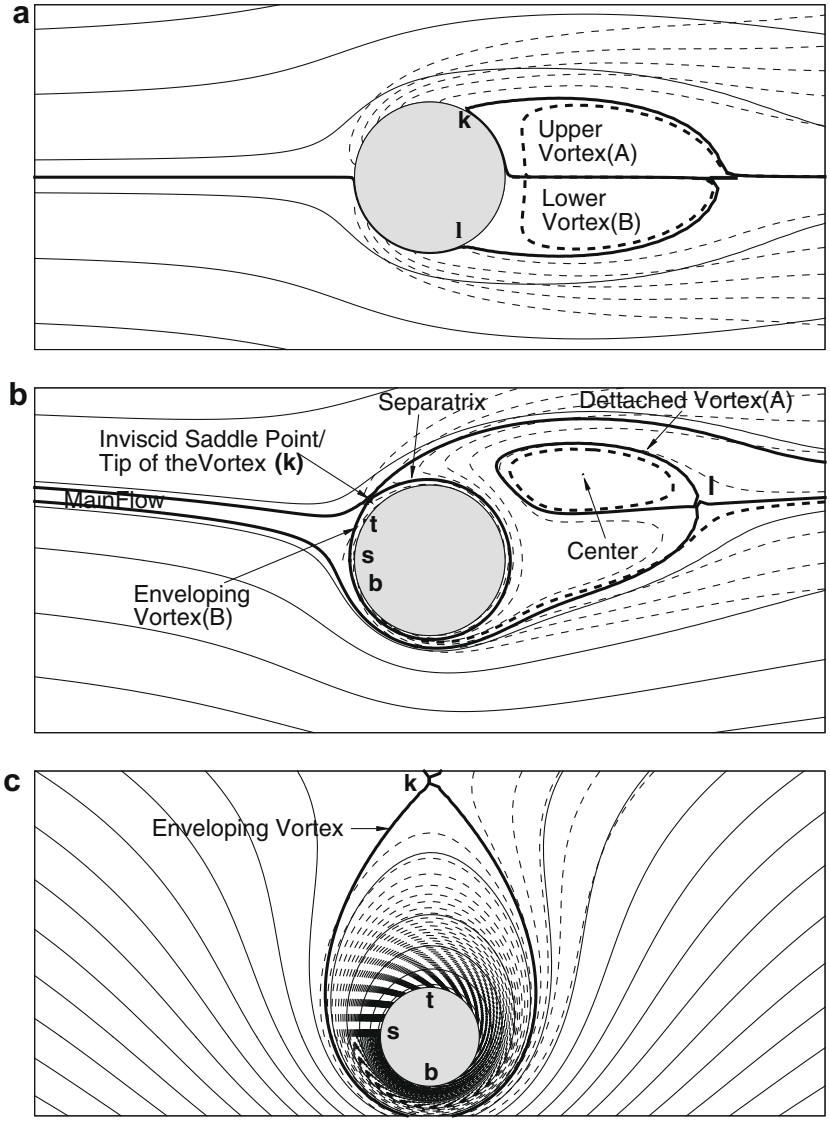

Fig. 3. Streamlines shown by solid and heatlines by dashed lines at Re = 40 for (a) stationary; (b) and (c) rotating cylinder at $\alpha = 1$ and 6, respectively.

from the cylinder surface with the loss of symmetry of the flow about horizontal centerline. Fig. 3(b) shows a separatrix which separates the incoming free stream main flow into two parts: one passing above the enveloping vortex and the other moving downward and around the enveloping as well as the detached vortices. At $\alpha \geqslant 3$ for all Re's considered here, the clockwise detached vortex in Fig. 3(b) disappears by merging into the flow and the flow contains only enveloping vortex with flow structure similar to potential flow theory, shown in Fig. 3(c) at $\alpha = 6$. Thus, at low to moderate α, the flow pattern near the cylinder is strongly affected by viscous forces but not at high α values with flow dominated by inertia effect. As in the case of stationary cylinder, here also there is flow acceleration and deceleration near the different portion of the cylinder surface resulting in favorable and adverse pressure gradient, from t-b and b-t in the direction of rotation, respectively, seen by the increasing or decreasing gap between the cylinder and enveloping vortex in Fig. 3(b) and (c). However, the flow inertia near the cylinder surface is sufficiently large to overcome the adverse pressure gradient with no flow separation on the cylinder surface.

For the stationary cylinder, the dashed lines in Fig. 3(a) shows that the heat lines/flow originates from the cylinder surface and extend/move downstream with decreasing heat flux indicated by increased gap between the two consecutive heatlines. Furthermore, as the heatlines are plotted here at a constant interval of heat-function, the increased gap over the cylinder surface indicates decreasing heat flux from the front to the rear end of the cylinder. At the rear end of the cylinder, it can also be seen that heat flows over twin recirculating heat/caloric-fluid flow regions, called here as twin "heat-vortex", detached from the cylinder. The heat flow is similar for the rotating cylinder, shown in Fig. 3(b) and (c), except that only one detached heat-vortex of smaller size than the fluid-vortex is formed at $\alpha = 1$ which also disappears at $\alpha \geqslant 3$, shown in Fig. 3(c) for $\alpha = 6$.

For a surface with tangential and normal coordinates as S_t and S_n, the Eqs. (12) and (13) for heatlines can be expressed as

$$\frac{\partial H}{\partial S_t} = \mathrm{Pe} U_n \theta - \frac{\partial \theta}{\partial S_n} \tag{12}$$

$$-\frac{\partial H}{\partial S_n} = \mathrm{Pe} U_t \theta - \frac{\partial \theta}{\partial S_t} \tag{13}$$

At the cylinder surface, S_t and S_n are along the angular and radial directions, respectively. For the cylinder surface maintained at CWT $\partial\theta/\partial S_t = 0$ and Eq. (13) reduces to $\partial H/\partial S_n = -\mathrm{Pe}\alpha$ as

$U_t = \alpha$ and $\theta = 1$. For stationary cylinder, $\partial H/\partial S_n = 0$ and thus, the heatlines are perpendicular to the wall for the stationary cylinder shown in Fig. 3(a). Due to rotation, the heatlines emerges more close to the cylinder surface angular direction which increases with increasing α as $\partial H/\partial S_n \to \infty$; i.e. $\partial H/\partial S_t \to 0$. Thus, the heatlines are tightly wound spirals with heat flow dragged by the cylinder rotation, released upward and finally swept away downstream by the fluid flow.

One interesting contribution of heatline pattern is that it shows graphically the magnitude of non-dimensional rate of heat transfer and can be directly used to obtain Nusselt number. The difference of heat function value between two consecutive heatline emerging from the surface gives the local heat transfer rate. The difference between maximum and minimum heatline values is equal to total heat transfer rate from the cylinder surface. Applying Eq. (12) at the surface where normal velocity, $U_n = 0$, the difference of heat function value between two consecutive heatline divided by the distance between them on cylinder surface gives $\partial H/\partial S_t$. This value is found to match with the local Nusselt number (not shown here). When the heatlines are plotted with a constant difference of heat function, the number of lines emerging from the cylinder surface indicates the relative magnitude of heat transfer rate. For example,

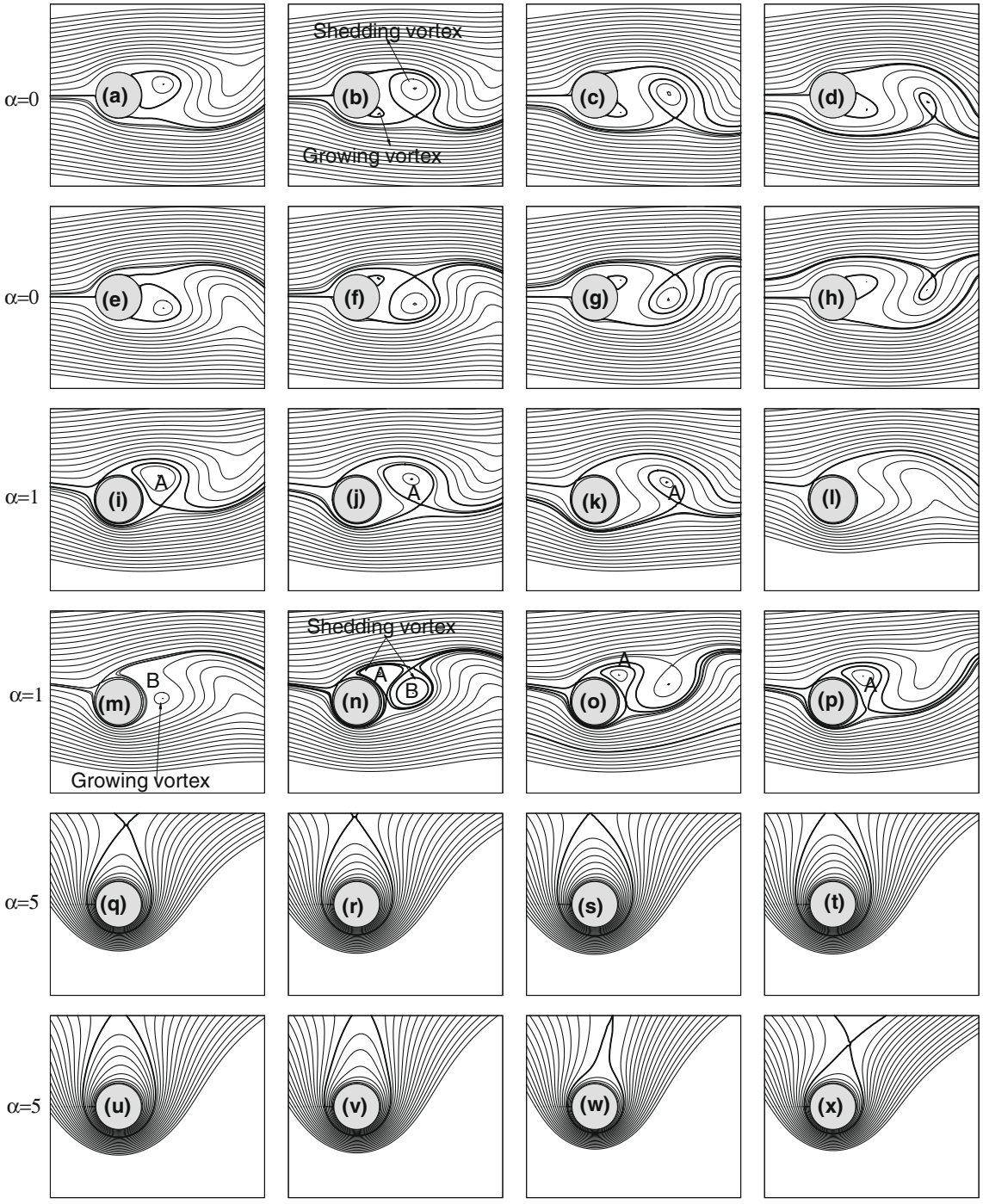

Fig. 4. Instantaneous streamlines near the circular cylinder, separated by an interval of one-eighth of the time period of vortex shedding, at Re = 100 for $\alpha = 0$, 1 and 5. Stream-function contours are at a constant spacing of 0.1.

there are 10 such lines for $\alpha = 1$ and 7 lines for $\alpha = 6$ in Fig. 3 indicating higher heat transfer rate for $\alpha = 1$. For $\alpha = 0$, Fig. 3 shows denser heatlines near the front end of cylinder whereas for $\alpha > 0$, denser heatlines are observed below the cylinder similar to the streamlines indicating higher heat flux.

6.3. Instantaneous fluid flow patterns in the VS regimes

The instantaneous streamlines in the Fig. 4 shows the detailed views of the laminar vortex shedding near the circular cylinder at Re = 100 for $\alpha = 0, \alpha = 1$ (I VS regime) and $\alpha = 5$ (II VS regime) for eight successive moments of time which span over the whole period. Thus, Fig. 4(a), (i) and (q) (corresponding to the time of maximum lift) is repeated after Fig. 4(h), (p) and (x), respectively for the next cycle of vortex shedding. In this figure, the critical points of the streamline patterns such as centers and saddles are shown with separatrix represented by thick line.

For stationary cylinder case, Fig. 4(a)–(h) shows only one growing and shedding vortex with the detachment of the growing vortex only after the shedding vortex disappears, resulting in not more than one shedding vortex at any time instant, (similar to that of Eaton [25]). However, for rotating cylinder, Fig. 4(i)–(p) shows an

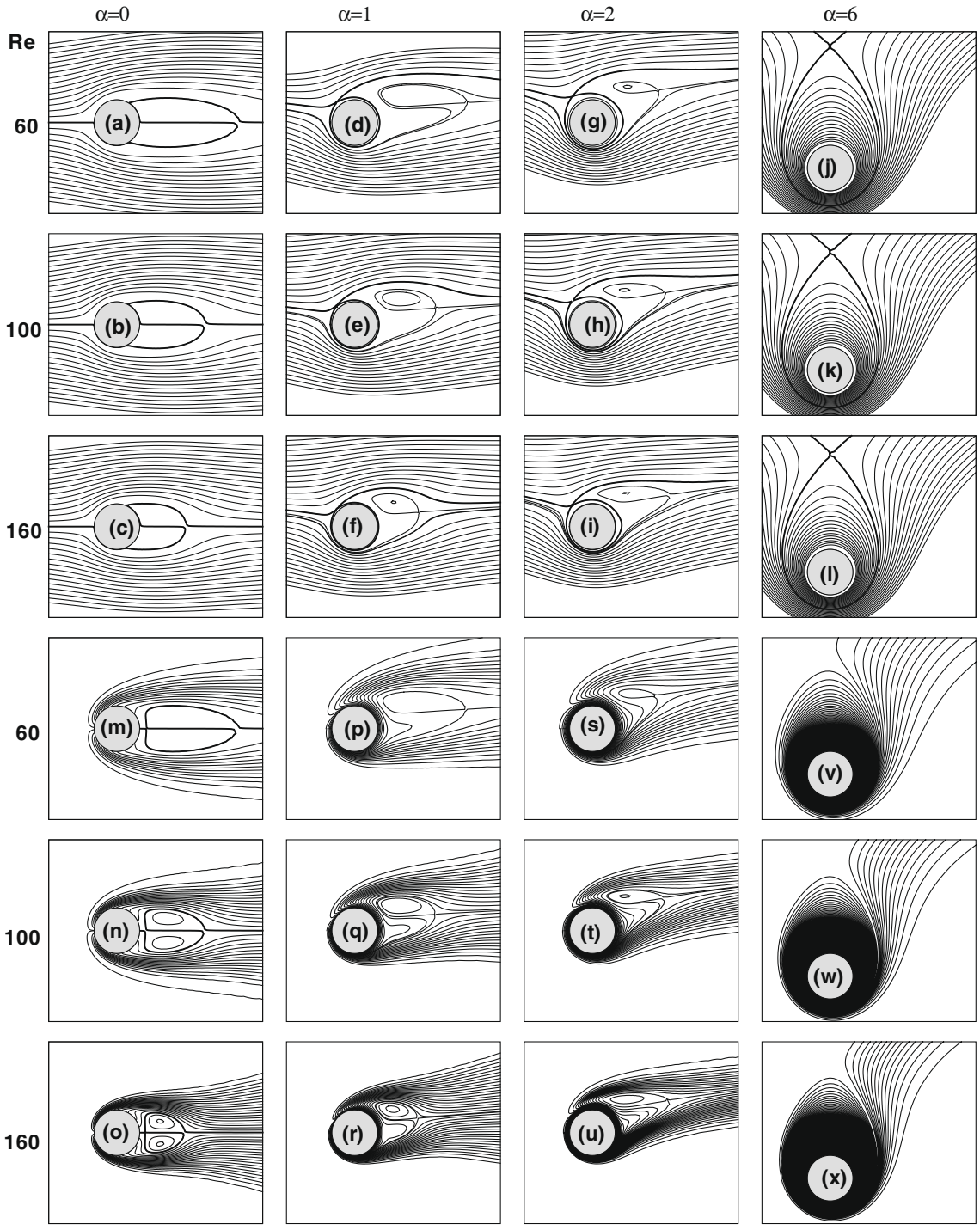

Fig. 5. Time-averaged streamlines (Fig. (a–l)) and heatlines (Fig. (m–x)) near the circular cylinder at Re = 60, 100 and 160 and rotation rate α of 0, 1, 2 and 6. Stream-function and heat-function contours are at a constant spacing of 0.1 and 0.5, respectively.

enveloping vortex and two growing/shedding vortices (Fig. 4(n) and (o)). In contrast to stationary cylinder, the seed for the shedding vortices are not formed on the cylinder surface but are formed in the flow field (compare Fig. 4(b) and (m)) and convected/shed downstream. Clockwise vortex "A" can be seen in all the figures of 4(i)-(p) except 4(l) and 4(m) in which it sheds out whereas anti-clockwise vortex "B" is visible only in Fig. 4(m) as growing vortex and Fig. 4(n) and (o) as shedding vortex. Therefore, as discussed earlier by Kang et al. [9], the clockwise vortex "A" is stronger and stays longer than the weaker anti-clockwise vortex "B". Moreover, it can be seen from Fig. 4(i)–(p) that the size of enveloping vortex remains constant.

Fig. 4(q)–(x) shows the instantaneous streamlines at a rotation rate $\alpha = 5$ which is in the II VS regime with much larger size of an egg shaped enveloping vortex and the disappearance of the clockwise detached vortex. The figure shows that the size/amount of enveloping vortex/recirculating-fluid varies with time. The decrease/increase in enveloping vortex size is related with the loss/gain of the fluid. The fluid moving around and below the vortex supply as well as take the fluid from the vortex for the time duration corresponding to Fig. 4(r)–(v). However, the flow above the vortex contributes only to the decrease in size of the vortex where the vortex releases the fluid from its tip at a time instant between Fig. 4(v) and (w). This tip of enveloping vortex performs an oscillatory motion with time. The vortex-shedding pattern is completely different at this rotation rate with one vortex shed in the transverse direction instead of two vortex shed in streamwise direction at $\alpha = 0$ and 1.

6.4. Steady/time-averaged heat and fluid flow patterns

Fig. 5(a)–(l) shows the streamlines and 5(m)-(x) shows the heatlines for various rotation rates and Reynolds number. Note that the results for $\alpha = 0$ and 1 are time-averaged as the flow is periodic. For the periodic flow, it can be seen that the size of twin/detached fluid (Fig. 5(a)–(f)) as well as heat (Fig. 5(m)–(r)) vortex decreases with increasing Re for the stationary/rotating cylinder. This indicates that the shedding vortex disappears at a shorter downstream distance with increasing Re at $\alpha = 0$ and 1. For steady flow at $\alpha = 2$, an opposite trend of variation of the size of the detached fluid/heat vortex with increasing Re is seen in Fig. 5(g)–(i)/(s)–(u), similar to that found in steady flow regime of stationary cylinder for twin vortex. However, the size of enveloping fluid-vortex decreases with increasing Re for periodic as well as steady flow across rotating cylinder, shown in Fig. 5(d)–(l). Thus, the amount of fluid inside the vortex increases with increasing Re and rotation rate.

6.5. Frequency and amplitude of unsteady periodic flow oscillation

The oscillation frequency is represented by Strouhal number and the oscillation amplitude by rms values of drag and lift coefficients, discussed in the following subsections for varying Re and varying rotation rate with the help of Fig. 6. Their values in y-axis on the left and right corresponds to range of α in the I and II VS regime, respectively, with zero values in the intermediate range of α as the flow is steady. Strouhal number is obtained here from temporal variation of lift coefficient.

In the I VS regime ($0 < \alpha < 2$), as the rotation rate increases from 0 to 1, Fig. 6(a) and (b) shows small change in St and C_{Lrms} whereas Fig. 6(c) shows rise in the value of C_{Drms} which increases with increasing Re. With further increase in rotation rate ($1 < \alpha < 2$), Fig. 6(a) shows slight drop in the values of Strouhal number and Fig. 6(b) and (c) show large drop in the C_{Lrms} and C_{Drms} indicating that the amplitude of vortex shedding approaches zero to reach to steady flow. Similar to stationary cylinder, Fig. 6 shows that the frequency and amplitude of vortex shedding flow increases monotonically with increasing Re for the cylinder rotating at a constant rotation rate. The maximum decrease in Strouhal number as α increases from 0 to α_I is 5.6% at Re = 160 whereas St increases by 38.5% at $\alpha = 0$ and 35.2% at $\alpha = 1$ as Re increases from 60 to 160. Thus, Strouhal number is strongly dependent on Re and weakly dependent on rotation rate in the I VS regime. Furthermore, in this regime, Fig. 6(a) shows an excellent agreement between the present result and that of Kang et al. [9], shown by filled symbols.

In the II VS regime for a very small range of increasing α (close to 5), Fig. 6(a) shows that the frequency of vortex shedding reduces from one-tenth to one-hundredth of its value in the I VS flow regime indicating that the unsteadiness is very slow. The large change in the frequency of the oscillation is due to entirely different periodic flow phenomenon in the I (Fig. 4(a–p)) and II (Fig. 4(q–x)) VS regimes. Fig. 6(b) and (c) shows that the rms value of lift and drag coefficient is greater in the II as compared to the I VS regime for all Reynolds numbers, probably due to large change in the size of enveloping vortex with time in the II VS regime (Fig. 4(v)–(x)).

6.6. Mean lift and drag coefficient

The pressure variation near the rotating cylinder (figure not shown here) indicated that the pressure is dependent on the gap between the cylinder and the enveloping vortex. Fig. 3(c) shows that the gap is minimum and thus, the velocity/pressure is maximum/minimum just below the cylinder and an opposite variation is found just above the cylinder. Thus, the pressure above the top half of the cylinder is more as compared to that in the bottom half resulting in the negative/downward pressure lift coefficient for the

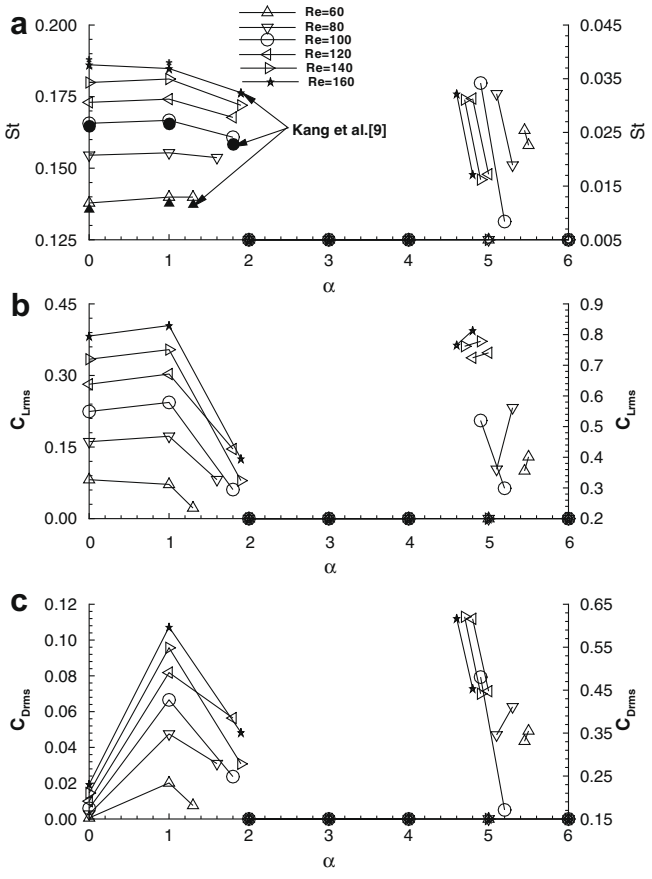

Fig. 6. Variation of (a) Strouhal number, (b) rms value of lift coefficient and (c) rms value of drag coefficient with increasing rotation rate α for various Re.

rotating cylinder, shown in Fig. 7(a). Furthermore, the figure shows monotonic decrease in the pressure lift coefficient with increase in rotation rate. This is due to the more increase in the size for the top half as compared to the bottom half of the enveloping vortex resulting in drastic reduction in the surface pressure values (figure not shown) on the lower half of the cylinder surface as compared to the reduction in the upper half at a constant Re whereas its increase with increasing Re at a constant α is marginal.

Fig. 7(b) shows that there is a monotonic decay in the pressure drag coefficient with increasing rotation rate with a change in the direction of the drag force around $\alpha = 2$. For $\alpha < 2$, Fig. 5(d)–(i) shows that the tip of the enveloping vortex (denoted by "k" in Fig. 3(c)) is in the front half of the cylinder. Thus, the area of fluid in the vortex and the pressure in the front half of the cylinder is more as compared to that in the rear half resulting in the positive/forward pressure drag coefficient for the cylinder rotating at $\alpha < 2$ and an opposite trend in the variation is found at higher rotation rate due to the change in the shape and size of enveloping vortex.

Fig. 7(a) shows that the negative/downward viscous lift coefficient and Fig. 7(b) shows the positive/forward viscous drag coefficient increases with increasing rotation rate due to increase in the velocity gradient at the cylinder surface. Fig. 7(c) shows that the downward lift force, $C_L = C_{Lp} + C_{Lv}$, increases monotonically with increasing α and with increasing Re. However, the increase is marginal with increasing Re. Thus, the lift coefficient is strongly dependent on rotation rate and weakly dependent on Re. Pressure force is found to contribute more to total lift force as compared to viscous force.

Fig. 7(d) shows the variation of total drag coefficient ($C_D = C_{Dp} + C_{Dv}$) with rotation rate α for all Re. For stationary cylinder, pressure drag contribute more to total drag. However, for rotating cylinder, the contribution of viscous drag increases sharply with increasing α and becomes more than that of pressure drag at the largest α, shown in Fig. 7(b). With increasing α, Fig. 7(d) shows that C_D decreases monotonically till certain rotation rate (around 4) and thereafter, it increases when an increasing trend of viscous drag dominates over the decreasing trend of pressure drag (Fig. 7(b)).

6.7. Local Nusselt number

Fig. 8 shows the variation of local Nusselt number on the surface of the cylinder with increase in the Re for various rotation rates α with the help of polar plot. Note that the scale in the radial direction is different in the sub-figures and innermost profile is at Re = 20 and outermost is at Re = 160.

For stationary cylinder, Fig. 8(a) shows that Nu_L increases with increasing Re where Nu_L is time averaged for Re = 60 to 160. Fig. 8(a) shows symmetric variation of Nu_L about $\phi = 180^\circ$ for all Re and kink in the Nu_L is seen at 180°. Nu_L is the maximum at $\phi = 0^\circ$ (front stagnation point) for all Re whereas it is minimum at 180° for Re = 20 and at two points $\phi_I \approx 130^\circ$ and at $\phi_{II} \approx 230^\circ$ for other Reynolds numbers. Furthermore, Nu_L decreases upto $\phi \approx \phi_I$, then $\phi_I < \phi \leqslant 180^\circ$ it increase, it again decreases $180^\circ < \phi \leqslant \phi_{II}$ and finally it increases for $\phi > \phi_{II}$, for Re = 40 to 160. For Re = 20, $\phi_I = \phi_{II} = 180^\circ$.

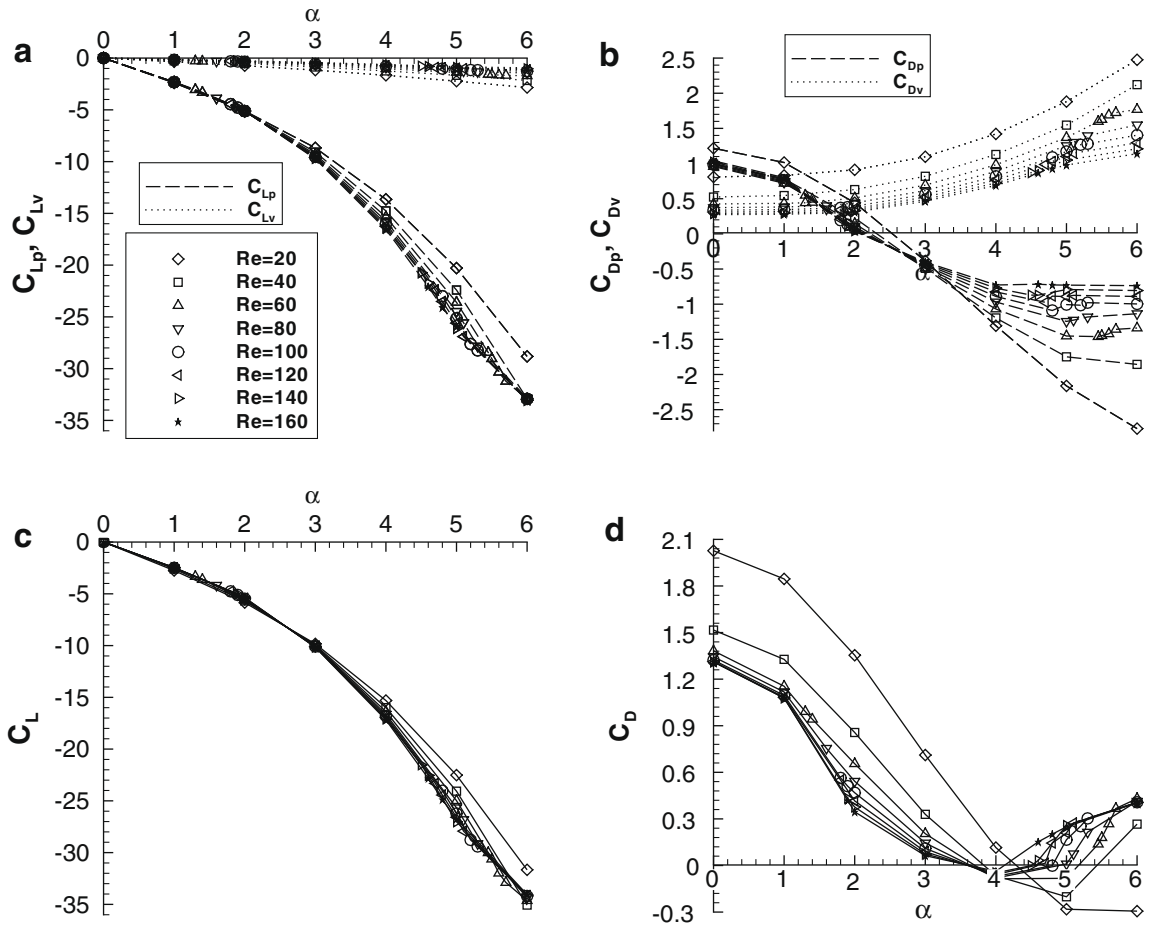

Fig. 7. Variation of (a) pressure and viscous lift coefficient. (b) Pressure and viscous drag coefficient. (c) Total lift coefficient. (d) Total drag coefficient with increasing rotation rate α for various Re.

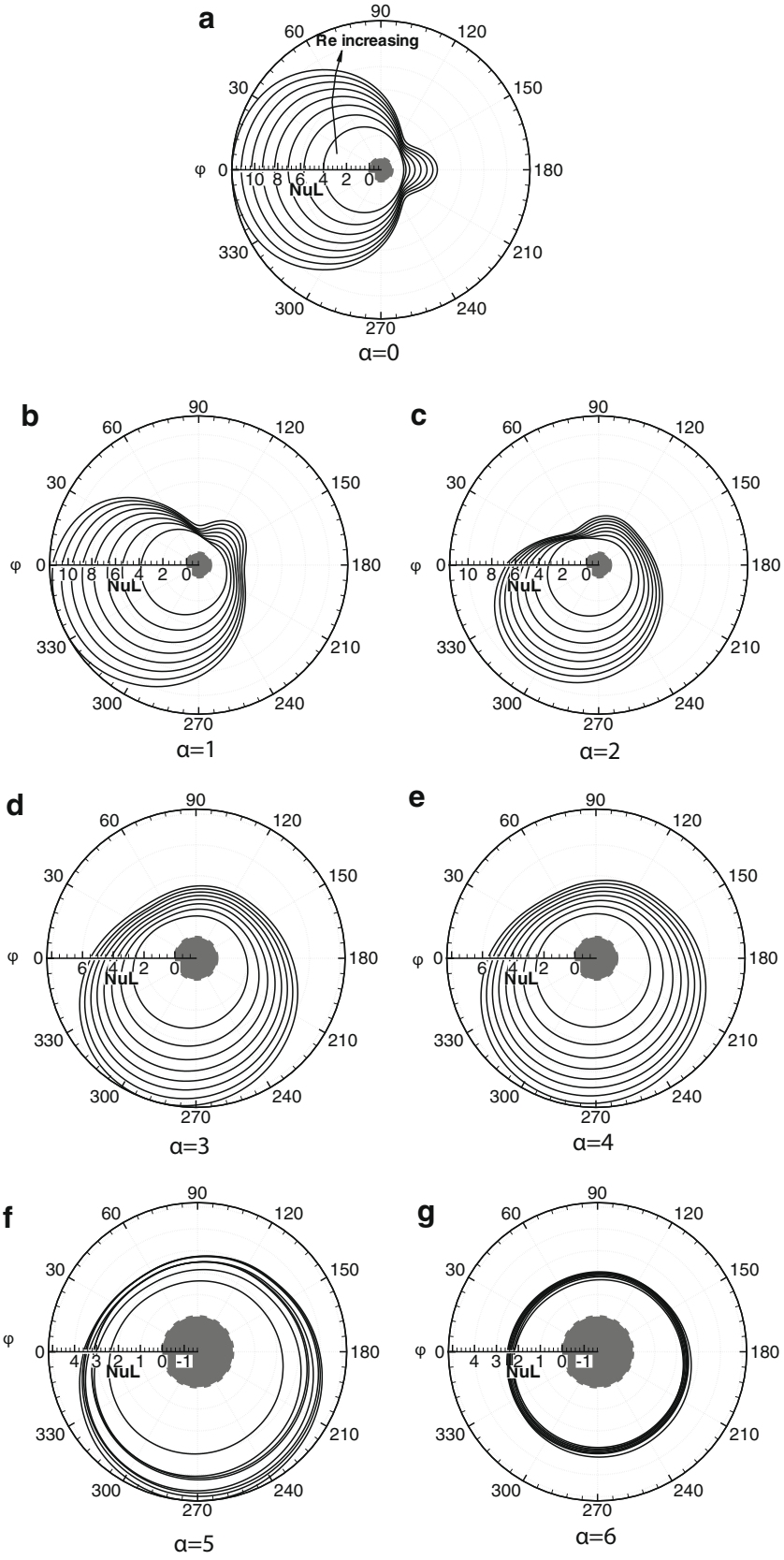

Fig. 8. Polar plot of local Nusselt number with increasing Re for various α.

For rotating cylinder, Fig. 8(b) shows the variation of Nu_L at $\alpha = 1$ where maximum in Nu_L does not occur at front stagnation point but shifts in the direction of rotation and is at $\phi \approx 325^\circ$. Minimum in Nu_L occurs at $\phi_I \approx 85^\circ$ and $\phi_{II} \approx 185^\circ$. Kink in Nu_L also shifts towards the direction of rotation. Further increase in rotation rate ($\alpha = 2$) shifts the maximum and minimum Nu_L further in the

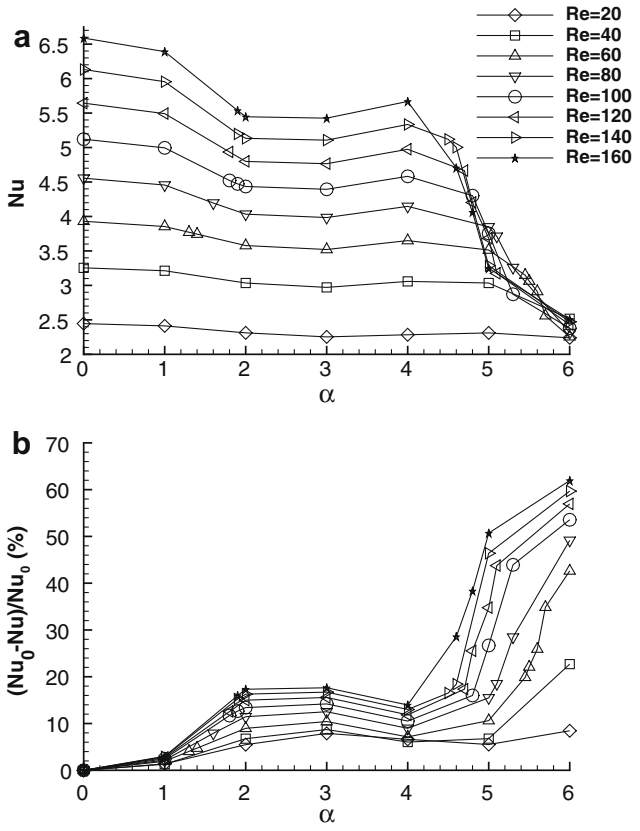

Fig. 9. Variation of (a) average Nusselt number and (b) percentage heat transfer suppression with increasing Re for various rotation rates α Nu_0 is the Nusselt number of stationary cylinder.

direction of rotation as seen in Fig. 8(c). For $\alpha = 3$ to 6 kink in Nu_L disappears and smooth variation in Nu_L is seen. The kink in Nu_L variation for $\alpha \leqslant 2$ may be related to the shape of the enveloping vortex which results in positive pressure drag (Fig. 7(b)). Fig. 8 shows that the variation in Nu_L for the range of Reynolds number decreases with increasing rotation rates. Furthermore, Nu_L becomes almost independent of Re at higher rotation rates as seen from Fig. 8(g). Moreover, figure also shows that the range of variation of Nu_L over the surface of the cylinder at a constant Re reduces with increase in α.

6.8. Average Nusselt number

For rotating cylinder maintained at Re = 100 and $\alpha = 1$, average Nusselt number of 4.991, obtained in the present study, matches well with 5.139 reported by Badr and Dennis [13]. Fig. 9(a) shows the variation of average Nusselt number and Fig. 9(b) shows the percentage suppression in heat transfer with increasing rotation rate for various Re. Fig. 9(a) show the monotonic decrease in the average Nusselt number with increasing rotation rates for various Re. The decrease in the Nusselt number with increasing rotation rate can be explained on the basis that the fluid entrapped inside the enveloping vortex acts as a buffer zone for heat transfer between the cylinder and free stream and restrict the heat transfer to conduction only. Furthermore, the size of enveloping vortex and thus, the mean thickness of the buffer zone increases with increase in α (figure not shown) resulting in the increase in the thermal resistance and decrease in conduction heat transfer. A drastic reduction in Nusselt number is seen in Fig. 9(a) for $\alpha > 4$, due to substantial increase in the size of enveloping vortex. The figure also shows that the Nusselt number increases monotonically with increasing Re at a constant α due to increased inertia of the flow. However, at the highest rotation rate of $\alpha = 6$, Nu reaches almost constant value around 2.5 for all Re i.e. becomes independent of Re. This is due to negligible change in the size of enveloping vortex with increasing Re and thus, the thermal resistance and Nu remains almost constant.

Fig. 9(b) shows the normalized Nusselt number obtained by the ratio of average Nusselt number of rotating cylinder to that of stationary cylinder for various rotation rates α to understand the suppression of heat transfer. It can be seen from the Fig. 9(b) that suppression increases with increasing Re and increasing α, having minimum of 8.44% in case of Re = 20 and maximum of 61.94% in case of Re = 160 at $\alpha = 6$. For the range of Re considered, the suppression of heat transfer is less than 20% for $\alpha \leqslant 4$ with a sharp increase for the higher rotation rates reaching a maximum of 61.94% in case of $\alpha = 6$ at Re = 160. Thus, cylinder rotation can be used not only for controlling flow but also as an efficient heat transfer suppression technique.

7. Conclusion

Present study focuses on the unconfined flow and heat transfer characteristics around a rotating circular cylinder in the 2-D laminar flow regime for various rotation rates and the cylinder subjected to constant wall temperature. Flow transition map found by the earlier researchers is shown here for a wider range of Reynolds number and rotation rates. With increasing in rotation rate for Re $\geqslant$ 60, suppression of vortex shedding takes place at certain α, thereafter, the vortex shedding reappears for a narrow range of α.

The heat flow is discussed with the help of heatlines using one of the earliest definition of heat as a caloric fluid with an analogy with streamline for fluid flow. For the stationary cylinder, the steady-state and time-averaged heat flow pattern represented by heatlines shows twin heat-vortex similar to fluid-vortex represented by streamlines in fluid flow. Heatlines emerges from the cylinder and passes over the heat-vortex of smaller size formed detached from the cylinder rear surface whereas the streamlines emerging from the free-stream inlet passes over the fluid-vortex attached on the surface. For the rotating cylinder, the steady-state and time-averaged streamlines shows an enveloping vortex and a detached vortex whereas the heatlines shows only a detached vortex of smaller size. Instead of enveloping fluid-vortex, the heatline emerges from the cylinder surface as tightly wound spirals with heat flow dragged by the cylinder rotation and released upward and finally swept away downstream by the fluid flow. At low rotation rates, the instantaneous streamline pattern during vortex shedding shows that the clockwise vortex stays much longer as compared to anti-clockwise vortex which leads to the formation of detached clockwise vortex in the time-averaged streamlines. However, the clockwise vortex is not seen at the higher rotation rates. Probably for the first time, the transient heat function is computed here in the finite-volume method framework as well as for the complex geometry/domain and is used to compute Nusselt number for CWT boundary condition.

The frequency of unsteady periodic flow decreases but its amplitude increases in the II VS regime as compared to the I VS regime. A downward lift force is found due to rotation which increases monotonically with increasing α and remain almost constant with increasing Re. Rotation can be used as a drag reduction technique as the drag coefficient decreases monotonically with increasing α upto 4 with a value close to zero at $\alpha = 4$ for all Re. Average Nusselt number is found to decrease with increasing rotation rate and increase with increasing Re, reaching almost a constant value at the highest rotation rate for all Re. Heat transfer

suppression due to rotation increases with increasing Re and increasing rotation rate.

References

[1] M.M. Zdravkovich, Flow Around Circular Cylinders, vol. 1, Oxford University Press, 1997.
[2] D. Barkley, D. Henderson, Three dimensional Floquet stability analysis of the wake of the circular cylinder, J. Fluid Mech. 322 (1996) 215–241.
[3] C.H.K. Williamson, Vortex dynamics in the cylinder wake, Ann. Rev. Fluid Mech. 28 (1996) 477–539.
[4] L. Baranyi, Computation of unsteady momentum and heat transfer from a fixed circular cylinder in laminar flow, J. Comp. App. Mech. 4 (2003) 13–25.
[5] P. Townsend, A numerical simulation of Newtonian and visco-elastic flow past stationary and rotating cylinders, J. Non-Newtonian Fluid Mech. 6 (1980) 219–243.
[6] H.M. Badr, S.C.R. Dennis, P.J.S. Young, Steady and unsteady flow past a rotating circular cylinder at low Reynolds numbers, Comput. Fluids 4 (1989) 579–609.
[7] D.B. Ingham, T. Tang, A numerical investigation into the steady flow past a rotating circular cylinder at low and intermediate Reynolds numbers, J. Comp. Phys. 87 (1990) 91–107.
[8] T. Tang, D.B. Ingham, On steady flow past a rotating circular cylinder at Reynolds numbers 60 and 100, Comput. Fluids 19 (1991) 217–230.
[9] S. Kang, H. Choi, S. Lee, Laminar flow past a rotating circular cylinder, Phys. Fluids 11 (1999) 3312–3321.
[10] D. Stojkovic, M. Breuer, F. Durst, Effect of high rotation rates on the laminar flow around a circular cylinder, Phys. Fluids 14 (2002) 3160–3178.
[11] D. Stojkovic, P. Schon, M. Breuer, F. Durst, On the new vortex shedding mode past a rotating circular cylinder, Phys. Fluids 15 (2003) 1257–1260.
[12] S. Mittal, B. Kumar, Flow past a rotating cylinder, J. Fluid Mech. 476 (2003) 303–334.
[13] H.M. Badr, S.C.R. Dennis, Laminar forced convection from a rotating cylinder, Int. J. Heat Mass Transfer 28 (1985) 253–264.
[14] G. Hu, D. Sun, X. Yin, B. Tong, Hopf bifurcation in wakes behind a rotating and translating circular cylinder, Phys. Fluids 8 (1996) 1972–1974.
[15] A.A. Kendoush, An approximate solution of the convection heat transfer from an isothermal rotating cylinder, Int. J. Heat Fluid Flow 17 (1996) 439–441.
[16] S. Kimura, A. Bejan, The 'heatline' visualization of convective heat transfer, ASME J. Heat Transfer 105 (1983) 916–919.
[17] A. Sharma, V. Eswaran, A finite volume method, in: K. Murlidhar, T. Sundararajan (Eds.), Computational Fluid Flow and Heat Transfer, Narosa Publishing house, India, 2003, pp. 445–483.
[18] S.B. Paramane, A. Sharma, Consistent implementation and comparison of FOU, CD, SOU and QUICK convection schemes on square, skew, trapezoidal, and triangular lid driven cavity flow, Numer. Heat Transfer B 54 (2008) 84–102.
[19] F.H. Barnes, Vortex shedding in the wake of a rotating circular cylinder at low Reynolds numbers, J. Phys. 33 (2000) L141–L144.
[20] F.L. Bello-Ochende, A heat function formulation for thermal convection in a square cavity, Comput. Meth. Appl. Mech. Eng. 68 (1988) 141–149.
[21] Q.H. Deng, G.F. Tang, Numerical visualization of mass and heat transport for conjugate natural convection/heat conduction by streamline and heatline, Int. J. Heat Mass Transfer 45 (2002) 2373–2385.
[22] V.A.F. Costa, Bejan's heatline and massline for convection visualization and analysis, ASME J. Heat Transfer 59 (2006) 126–145.
[23] A. Dalal, M.K. Das, Heatline method for the visualization of natural convection in a complicated cavity, Int. J. Heat Mass Transfer 51 (2008) 263–272.
[24] A.E. Perry, M.S. Chong, T.T. Lim, The vortex shedding behind two-dimensional bluff bodies, J. Fluid Mech. 116 (1982) 77–90.
[25] B.E. Eaton, Analysis of laminar vortex shedding behind a circular cylinder by computer-aided flow visualization, J. Fluid Mech. 180 (1987) 117–145.